ACS APPLIED NANO MATERIALS

www.acsanm.org Article

Selective and Practical Graphene-Based Arsenite Sensor at 10 ppb

Sourav Kanti Jana,[†] Kamalesh Chaudhari,[†] Md Rabiul Islam, Ganapati Natarajan, Tripti Ahuja, Anirban Som, Ganesan Paramasivam, Addanki Raghavendra, Chennu Sudhakar, and Thalappil Pradeep*

Cite This: *ACS Appl. Nano Mater.* 2022, 5, 11876−11888 Read Online

ACCESS | Metrics & More | Article Recommendations | Supporting Information

ABSTRACT: Arsenic detection in field water samples at concentrations of relevance with affordable and simple equipment is of global interest. We report a biomimetic electrode using electrochemically reduced graphene oxide (ERGO) for highly selective and sensitive reagent-free arsenite (As^{3+}) detection in field water samples, down to the ten parts per billion level, enabling measurement of drinking water quality affordably for millions of arsenic-affected people. This electronically and structurally optimized ERGO electrode shows selective detection of As^{3+} in both phosphate buffered saline (PBS, pH ∼7) and field water samples, even though more than 100 times larger conductivity and total dissolved solids (TDS), respectively, are present in them. Raman and FTIR spectroscopies were used to understand the mechanism of selectivity and sensitivity. The sensing mechanism involved two processes, namely, selective binding of As^{3+} with the −COOH groups of ERGO followed by its electro-oxidation by an applied potential. Density functional theory (DFT) and force-field calculations were used to obtain crucial insights into the site selectivity and mechanism of oxidation of As^{3+}. A two-electron transfer process from As^{3+} to ERGO followed by associative O ligand addition to As^{3+} by a ketone oxygen atom, and concomitant regeneration of −COOH group is presented. The ion selectivity depends both on structural and electronic factors. First, the compact pyramidal-shaped As^{3+} species may closely approach the edge −COOH functional group to a greater extent than the other ions enabling covalent binding of the As center with the ketone O atom. Furthermore, closer proximity of the lowest unoccupied molecular orbital (LUMO) acceptor level of the positively charged ERGO and the highest occupied molecular orbital (HOMO) donor level of the As^{3+} species suggests that a uniquely selective resonant charge-transfer effect occurs between the As^{3+} species and ERGO.

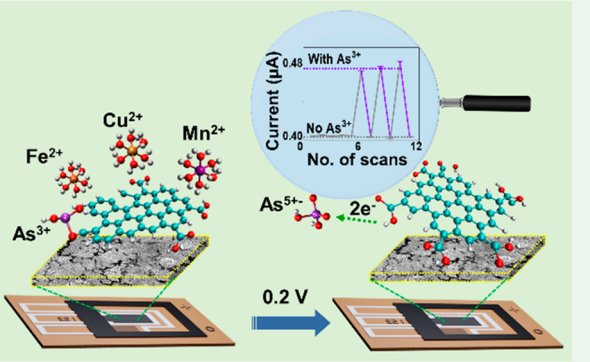

KEYWORDS: *graphene, ERGO, biomimic device, arsenic sensor, chronoamperometry, electron transfer, density functional theory, Raman spectroscopy*

INTRODUCTION

Availability of clean water (CW) globally necessitates continuous monitoring of water sources and service lines. Development of reliable, cost-effective, and compact sensors for water quality is thus an important need.[1] Biosensors offer high sensitivity and selectivity to specific contaminates with a quick response time and regenerability.[2−4] Enzymes have been used extensively as active constituents of biosensors for the detection of contaminants, especially in the biological context.[5−7] For example, glucose oxidase (GOx) is commonly used for rapid screening of the glucose concentration in human blood, for diabetes management.[8] Arsenic (As), a notorious natural poison, found in many water bodies and one of the world's deadliest environmental hazards, affecting over 300 million people globally, can be detected by an enzyme, arsenite oxidase (AiO). Long-term consumption of arsenic contaminated drinking-water and food can cause skin lesions and even cancer. It has also been associated with cardiovascular disease and diabetes. It impairs cognitive development. Specific additional health effects include hyperpigmentation, keratosis, anemia, burning sensation of eyes, liver fibrosis, chronic lung disease, and neuropathy. Therefore, its quantitative and selective detection in drinking water with an affordable device like a glucometer is essential. Elemental As exists in two ionic forms, arsenite (As^{3+}) and arsenate (As^{5+}), in natural water and the former is more toxic.[9−12] AiO immobilized electrode was shown to be capable of detecting As selectively in water.[9] As^{3+} binds with the molybdenum (Mo) center of AiO thorough nucleophilic interaction and subsequently, As^{3+} is oxidized by the concurrent reduction of molybdenum of AiO (Mo^{6+} to Mo^{4+}) during the catalytic cycle.[9,13] Despite its selectivity to As^{3+}, its complex extraction and purification procedure,

Received: July 1, 2022
Accepted: August 8, 2022
Published: August 17, 2022

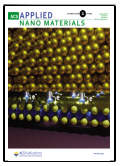

stability at ambient temperatures, and more importantly, binding to a particular substrate inhibit the use of AiO for field applications as of now.[14,15]

Several chemical entities such as metal complexes, porphyrins, fullerene derivatives, gold nanoparticles, and rare earth nanoparticles that exhibit structural diversity (size, shape, and morphology), specific crystallographic orientation, and surface charge have been shown to mimic various natural enzymes.[16−18] Currently, As^{3+} sensing using nanomaterials is exclusively based on anodic stripping voltammetry (ASV).[19−23] Efforts to synthesize different nanostructured materials, with an aim of developing a biomimetic electrode with activity similar to AiO but with superior physical and chemical stability has been reviewed.[24] The performance of most of these materials for selective As^{3+} sensing in natural water samples, composed of numerous other species, typically at several orders of magnitude larger concentrations, is not satisfactory for field-deployment. Thus, the need to develop an electrode for selective As^{3+} sensing is obvious.

Although reduced graphene oxide is a common material now-a-days, controlled modulation of functional groups and subsequent changes in its electronic properties are expanding areas of research for developing chemical/biological sensors, especially for toxic metal ions in water. Graphene oxide (GO) and reduced graphene oxide (rGO) have found applications in biomimetic chemistry because of the presence of various functional groups that can interact with a wide range of target molecules through different binding mechanisms.[25,26] Moreover, rGO was shown to possess greater affinity toward target molecules than even natural enzymes because of the higher synergetic effect due to its high surface area and electronic conductivity.[27−29] Electronic properties of rGO can be tuned by modifying the oxygen-containing functional groups. Such tunable electronic properties and surface charge of rGO facilitated its application as biosensors.[30] In view of that, we have fabricated an rGO-based arsenite sensor.

Here we report an electrode composed of a few layers of electrochemically reduced graphene oxide (ERGO) as an alternative to AiO for selective and sensitive As^{3+} sensing, in natural waters. Tailoring the functional groups of the ERGO film in a controlled fashion is imperative to mimic the characteristics of AiO. We propose an approach to bind the arsenic species with the functional groups of ERGO and subsequent oxidation of the bound species at the surface upon application of a potential. Various electro-analytical and spectro-electrochemical measurements were employed to understand the biomimetic activity of the ERGO electrode. Spectroscopic studies confirmed that As^{3+} binds with −COOH functional groups, which resulted in a change in the molecular orientation of ERGO. These bound species were oxidized at the surface of the electrode and released from the surface as As^{5+} after application of a potential. These processes and the selectivity mechanism of the sensor toward different ions were modeled computationally.

MATERIALS AND METHODS

Chemicals. Flexible gold (Au) strips were purchased from Bio Nano Consulting (BNC), London, UK. Approximate thickness of Au was maintained as 10 nm over polyethylene terephthalate (PET) substrate. Sodium 2-mercaptoethanesulfonate (MESA, $HSCH_2CH_2SO_3Na$) of 99.9% purity was purchased from Sigma-Aldrich and it was used for surface modification of Au strips. For the synthesis of GO using modified Hummer's method, we used several chemicals. Graphite flakes (95% of carbon) were obtained from Active Carbon India Pvt. Ltd. Sulfuric acid (H_2SO_4, 95−98%), hydrochloric acid (HCl, 36%), ammonia (NH_3, 30%), and hydrazine hydrate (N_2H_4. H2O), were obtained from Rankem Chemicals Pvt. Ltd., India. Hydrogen peroxide (H_2O_2, 98%) was purchased from Merck, India, and phosphorus pentoxide (P_2O_5, 95%) was from SD Fine Chemicals Pvt. Ltd., India. Sodium nitrate ($NaNO_3$) was procured from Loba Chemie, India. Potassium peroxydisulfate ($K_2S_2O_8$, 98%) and potassium permanganate ($KMnO_4$, 98.5%) were bought from Sisco Research Laboratories Pvt. Ltd., India. Detailed synthesis process of GO is described in the Supporting Information. The experimental procedure including detailed synthesis of ERGO electrodes, followed by their morphological and structural characterization and study of As^{3+} sensing via several electroanalytical and in situ spectroelectrochemical techniques, is shown in Figure S1.

Electrode Fabrication. The complete fabrication process of ERGO electrodes comprised the synthesis of GO by modified Hummer's method,[31] pretreatment of Au strips with sodium 2-mercaptoethanesulfonate (MESA), coating of GO on Au strip by the drop cast method, and finally electroreduction of the GO film. Each of these steps is described in detail in the Supporting Information. We prepared three different ERGO electrodes by varying the electroreduction time (1, 3, and 6 h) of GO coating over flexible Au strips and the samples were named accordingly (ERGO1, ERGO3, and ERGO6, respectively).

Instrumentation. Surface morphology and elemental analysis of the electrodes were performed by FESEM−EDX (Thermo Scientific Verios G4 UC). Backscattered electrons and secondary electrons were used for imaging at an accelerating voltage of 10 kV under high vacuum condition.

Raman spectroscopy was performed on ERGO1 and ERGO6 using a confocal Raman instrument (Witec GmbH, Alpha-SNOM alpha300S) equipped with a 633 nm laser (power ∼10 mW) as the excitation source. Raman spectra were collected for electrodes in air and in the presence of DI water. In-situ spectro-electrochemical measurements were carried out using electrodes in the presence of As^{3+} mixed with DI water. Electrode strips were connected with an electrochemical workstation through a strip holder, which was mounted on a piezoelectric scan stage of the Raman spectrometer. Measurements were carried out with a 20× objective (Plan-Apochromat, Zeiss) for solid state measurements. Spectro-electrochemical measurements were carried out using a 60× water objective (Nikon Fluor). Spectro-electrochemical measurements were performed using an EMSTAT potentiostat, in presence and absence of a DC potential, with 100 μL of aqueous As^{3+} solution on both the electrodes. The spectra were collected at the laser excitation wavelength with an acquisition time of 1 s. A long band-pass filter was placed in the path of the Raman signal, to cut off the Rayleigh scattering. The signal was then dispersed using a 600 grooves/mm grating, and finally, the dispersed light was collected with a Peltier-cooled charge coupled device.

IR spectra of ERGO electrodes were acquired by a PerkinElmer FT-IR spectrometer. All the electrodes were dried completely under vacuum condition before performing IR measurements.

X-ray photoelectron spectroscopy (XPS) measurements were carried out using an Omicron Nanotechnology ESCA probe TPD spectrometer. Polychromatic Al Kα was used as the X-ray source ($h\nu$ = 1486.6 eV). All the ERGO samples were placed on a carbon tape attached on the sample stub. Constant analyzer with energy of 20 eV was used during measurements. Prior to measurements, binding energy was calibrated with respect to C 1s at 284.8 eV. All the XPS spectra of the samples were deconvoluted using CasaXPS software.

Electroanalytical Measurements. Change in electronic conductivity and interfacial transport property of ERGO samples were investigated by electrochemical impedance spectroscopy (EIS). Surface charge of ERGO electrodes was studied using Mott−Schottky (M-S) analysis and the interfacial (electrode/electrolyte) electron transport property was evaluated using the Nyquist plot. M-S analysis was performed by measuring impedance of each electrode by varying applied DC potential at a given frequency of the AC signal (in our

https://doi.org/10.1021/acsanm.2c02860
ACS Appl. Nano Mater. 2022, 5, 11876−11888

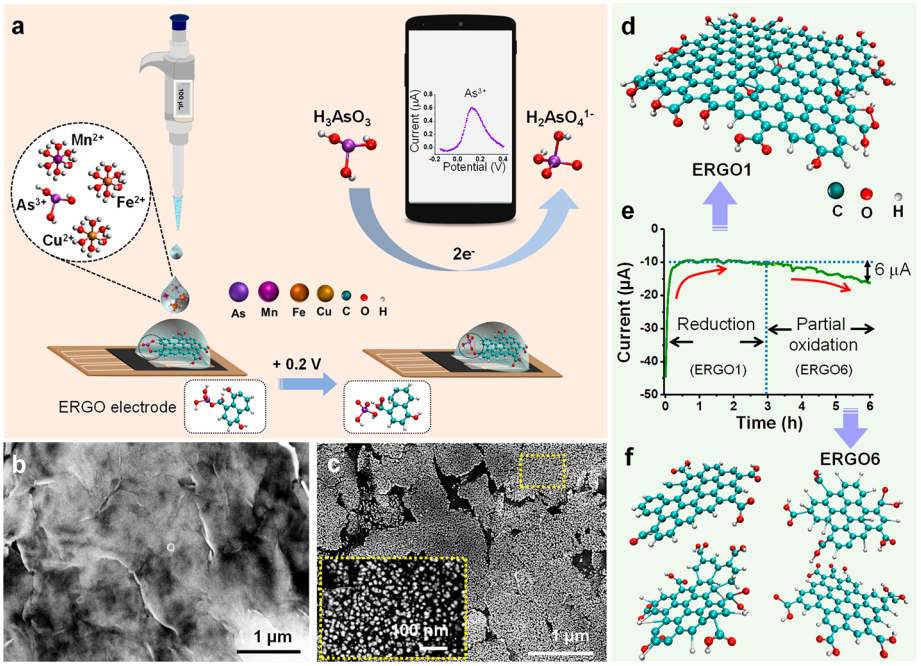

Figure 1. (a) Schematic representation of selective As^{3+} sensing by ERGO electrode. The geometric area of the working electrode is ~0.2 cm^2 (0.7 cm × 0.3 cm). FESEM images of (b) ERGO1, (c) ERGO6 electrode at the same magnification. Inset of Figure 1c shows a magnified FESEM image of the chosen area. Figure 1d, f represent changes in the molecular structure of ERGO during the electroreduction process. Figure 1e corresponds to the chronoamperometry (CA) curve of electroreduction during the preparation of ERGO strips. Here, current decreased from −45 to −10 μA within 15 min and it remained constant up to 3 h, implying electroreduction of the oxygen-containing functional groups (C−O, C−OH). Afterward, it started to increase slowly from −10 to −16 μA, which could be attributed to the breaking of a large sheet into small nanosheets and the edges of ERGO6 nanosheets being oxidized. Figure 1f represents the molecular structure of ERGO6, which suggests that the top surface of ERGO6 consists of several nanosheets, in agreement with the SEM image in c.

case, it was 1 kHz), while Nyquist plot was deduced by measuring impedance of the electrodes in the frequency range of 5 MHz to 100 Hz. Amplitude of the signal was maintained as 10 mV during measurements. Both measurements were performed in the presence of phosphate buffered saline (PBS). Electroanalytical measurements with ERGO electrodes were carried out via cyclic voltammetry (CV), linear sweep voltammetry (LSV), and chronoamperometry (CA) measurements in PBS and field water samples for As^{3+} sensing. The sensing mechanism was further analyzed by in situ electrochemical measurements with Raman and FTIR spectroscopy. Experimental details are presented in detail in the Supporting Information.

DFT Calculations. We modeled the analyte−sensor binding interaction, oxidation mechanism, and the selectivity of the sensor toward different analyte ions using density-functional theory (DFT) calculations and our methods are described in detail in the Supporting Information.

RESULTS AND DISCUSSION

Biomimetic activity of ERGO electrode with exceptional sensitivity and selectivity toward As^{3+} is displayed schematically in Figure 1a. As^{3+} binds selectively with the acid functional group of ERGO and upon application of a low DC potential, it was oxidized and released as As^{5+} into the solution. In this process, a signal was detected and active sites were regenerated. Therefore, it is necessary to analyze the change in structural and electronic properties, brought about by tailoring the surface functional groups of the active ERGO electrode.

Morphological and Structural Evolution of the ERGO Electrodes. ERGO samples were prepared by electroreduction of GO coated Au strips at −1.1 V. Electroreduction was performed for different time periods (1, 3, and 6 h) and corresponding electrodes were labeled as ERGO1, ERGO3, and ERGO6, respectively. Surface morphology of these ERGO electrodes and structural changes upon electrochemical reduction can be seen from FESEM micrographs. Morphology of ERGO1 resembled that of a continuous wrinkled thin film (Figure 1b). On the other hand, ERGO6 (Figure 1c) was composed of many smaller sheets with varying sizes (~1−2 μm). Moreover, an expanded SEM image (inset of Figure 1c) showed that each ERGO6 sheet was an assembly of smaller particles of reduced graphene oxide, having particle sizes in the range of ~10−20 nm. Additional SEM images and detailed EDS analysis of ERGO6 is presented in Figure S2. EDS spectrum (Figure S 2d) taken from one of these small particles confirms the elemental composition (carbon C and oxygen O). Presence of fluorine (F) is associated with Nafion, used as a binder for electrode fabrication.

XPS analysis was performed to study the possible changes in elemental composition during the electroreduction process. We carried out this analysis on GO, ERGO1, and ERGO6. XPS spectra of C 1s and O 1s of all the electrodes are shown in Figure S3. The C 1s region of GO, ERGO1, and ERGO6 samples are shown in Figure S3a−c and O 1s spectra are shown in Figure S 3d−f, respectively. Spectral features of deconvoluted C 1s and O 1s peaks are presented in Table S1, and are in agreement with the reported values.[32−34] Before electroreduction, population of oxygen containing functional groups of GO was higher than in ERGO samples. After the electroreduction process, a significant decrease in the population of oxygen-containing functional groups, especially of hydroxyl and epoxy groups, was observed from parent GO. Population of O−C═O functional groups was similar for both ERGO1 and ERGO3. Surprisingly, an increase in the

https://doi.org/10.1021/acsanm.2c02860
ACS Appl. Nano Mater. 2022, 5, 11876−11888

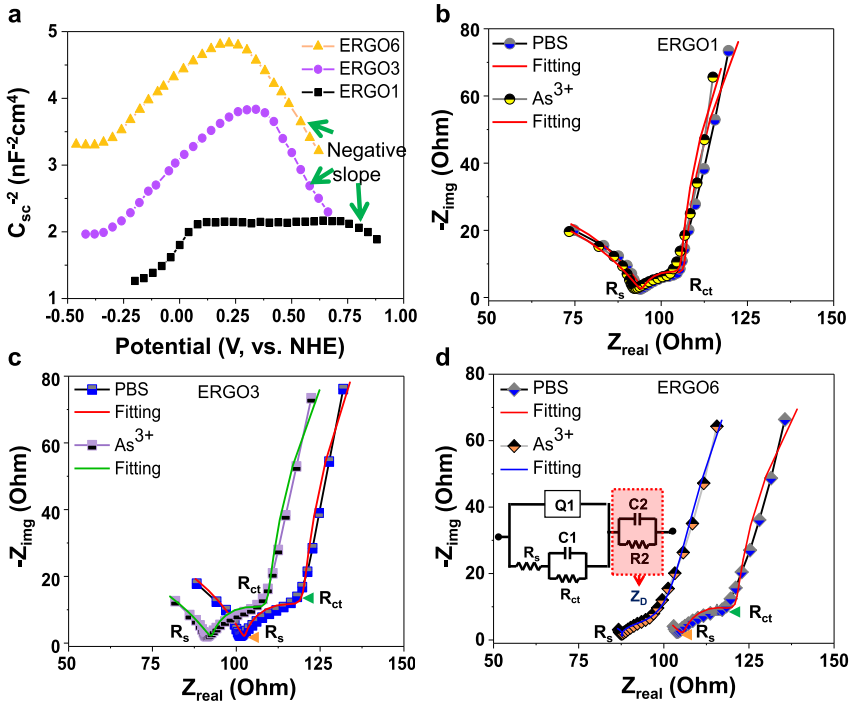

Figure 2. (a) Mott−Schottky analysis of ERGO samples to determine surface charge of the electrodes. Nyquist plots of different ERGO samples with and without As^{3+}, (b) ERGO1, (c) ERGO3, and (d) ERGO6. The equivalent electrical circuit, which was deduced after fitting the impedance spectra of all the electrodes, is shown in the inset of Figure 2d. The value of each fitting circuit elements is shown in Figure S4c.

population of C═O and C−O functional groups was observed for ERGO6, compared to ERGO1, as seen in Figure S3d−f. This was attributed to the reoxidation of ERGO during electrode preparation, as noticed from the CA profile (Figure 1e). The electroreduction current reached a constant value within 15 min and remained unchanged up to 3.5 h. Beyond this point, the current started increasing, indicating partial reoxidation and at 6 h, the current was maximum. This enhanced current signified that a continuous larger sheet structure got fragmented into tiny sheets, which remained assembled (Figure 1c). Figure 1d, f show schematic representations of the molecular structures of ERGO1 and ERGO6, respectively. Therefore, initial reduction and subsequent controlled oxidation in ERGO6 optimized the size and functional groups present on the surface, which further modulated the surface electronic conductivity, and interfacial transport property, thereby enabling sensitive and selective As^{3+} sensing.

Change in Electronic Conductivity and Interfacial Charge Transport Property of ERGO. The presence of different functional groups such as hydroxyl and carboxyl made GO negatively charged in solution. During electroreduction, some of these functional groups present at the surface of the electrode were reduced, which was expected to enhance the electron density at the edges of ERGO. Thus, electronic conductivity of the electrodes got enhanced.[35] Electronic properties including surface charge densities of each of the ERGO electrodes were investigated by Mott−Schottky (M-S) analysis performed at 1 kHz, in which reciprocal of the square of capacitance was plotted as a function of the potential applied to the electrodes.[35] M-S profiles of all three ERGO electrodes are shown in Figure 2a. Prominent inverse V shaped M-S profiles were observed for both ERGO3 and ERGO6 confirming simultaneous existence of both positive and negative charges on the electrodes.[36,37] A higher negative slope observed for these two indicated greater accumulation of positive charges (H^+ or H_3O^+) at the edges, compared to ERGO1 in the aqueous medium, since the dielectric constant was similar for all the electrodes (Figure S4a). They formed Stern Layers at the surface of the respective electrodes, when the electrodes were dipped into an aqueous solution. ERGO6 was found to possess a higher charge density compared to the other two electrodes, with positive charge density being dominant over negative charge density (Figure S4b). This made ERGO6 highly protonated (H^+ /H_3O^+) and p-type (positively charged) in solution.

To understand the interfacial charge transfer property of individual ERGO electrode at the electrolyte interface, we measured total impedance of each electrode by varying the frequency of the AC signal at a constant DC potential of 0.1 V. Figure 2b−d represent the Nyquist plots of ERGO1, ERGO3, and ERGO6, respectively, before and after exposure to As^{3+}. Each experimentally obtained Nyquist spectrum was fitted with the impedance spectrum of an equivalent electronic circuit (inset of Figure 2d). In Nyquist plots, it is seen that each semicircle has two intercepts to the *X*-axis, first of which corresponds to the equivalent series resistance (R_s) and the second one indicates the charge transfer resistance (R_{ct}). R_s is associated with combined effect of solution conductivity and bulk electronic property of ERGO while R_{ct} is related to charge transfer kinetics at the ERGO/electrolyte interface. C1 corresponds to the space charge capacitance. Q1 represents an impedance which is the combination of interfacial resistances and capacitances of porous electrode material, and the combination of C2 and R2 constitutes an impedance representing the bulk diffusion of ions toward the interface of the electrode and into the porous network of the electrode. Before the addition of As^{3+} to the electrolyte, an increasing

https://doi.org/10.1021/acsanm.2c02860
ACS Appl. Nano Mater. 2022, 5, 11876−11888

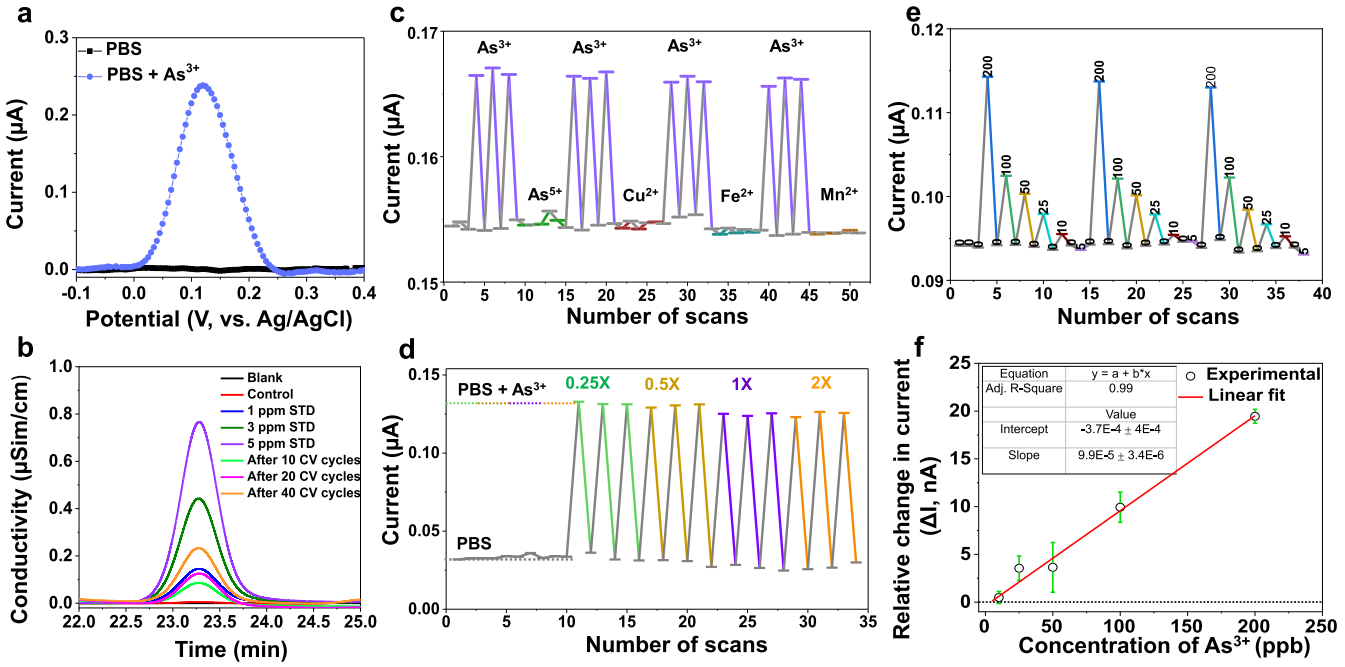

Figure 3. (a) LSV response of ERGO6 without and with 1 ppm As^{3+}, (b) Chronograms obtained from ion chromatography (IC) measurement with the solutions obtained after different number of CV cycles and same measurement with standard (STD) As^{5+} solutions of different concentrations. (c) Interference study performed with several heavy metal ions with ERGO6 electrode. Concentration of As^{3+} was fixed at 200 ppb, while 1 ppm was maintained for interfering ions. (d) Investigation of CA current response of 1 ppm As^{3+} spiked in PBS with different ionic conductivity. We prepared PBS solutions of different conductivity by changing their ionic concentrations and used them further as electrolytes during CA measurements. (e) CA measurement with different concentrations of As^{3+}. (f) Calibration curve showing linearity down to 10 ppb.

trend in R_s (90 Ω to 104 Ω) with increasing electroreduction time of ERGO samples (ERGO1 to ERGO6) was observed. However, with an increase in electroreduction time, R_s of ERGO was expected to decrease as the conductivity of the electrode increased. This anomaly was presumably due to the accumulation of higher positive surface charge (H^+) at the surface of ERGO (ERGO3 and ERGO6), which increased the space charge capacitance at the interface of electrodes, between the current collector and active electrode (Au/ERGO), as well as between the electrode and electrolyte (ERGO/PBS). These space charge capacitances tend to increase R_s. In presence of As^{3+}, value of R_s did not change. This is likely due to insufficient positive charge accumulation at the surface of ERGO1, which could not facilitate the electrostatic interaction between the $As(OH)_3$ moiety and the ERGO1 surface. However, the presence of higher positive surface charge on ERGO3 and ERGO6, enabled these electrodes to bind with $As(OH)_3$. Adsorption of As^{3+} on ERGO3 and ERGO6 decreased the space charge capacitance, leading to a reduction in R_s for both. No significant change in R_{ct}, even after exposure of As^{3+}, was observed for ERGO1 and ERGO3, whereas a decrease (from 15 Ω to 7 Ω) could be seen in the case of ERGO6. This decrease in R_{ct} implies that electron transfer happens at the ERGO6/electrolyte interface through faradaic reaction. Impedance spectroscopy results thus reveal that ERGO6 alone is sensitive to As^{3+}.

Selectivity and Sensitivity of ERGO6 Electrode toward As^{3+}. To be considered as a biomimetic electrode for As^{3+} sensing, an electrode has to exhibit high sensitivity and selectivity toward As^{3+}. Further, the ionic conductivity and total dissolved solids (TDS) of the electrolyte medium should not affect the As^{3+} response of the electrode, for it to be used in the field. To demonstrate the sensitive and selective detection of As^{3+} with ERGO6 electrode, we employed electroanalytical measurements [cyclic voltammetry (CV), linear sweep voltammetry (LSV) and chronoamperometry (CA)].

Sensitivity. The sensitivity of the ERGO6 electrode toward As^{3+} was evaluated by LSV using 1 ppm of As^{3+}. Corresponding voltammogram showed a peak at 0.1 V (Figure 3a) due to the electro-oxidation of As^{3+} at the surface of ERGO6. CV was performed with all the ERGO electrodes using same concentration of As^{3+}, and only ERGO6 electrode responded to As^{3+} (Figure S5). In the CA profile (Figure S6a), the initial ten data points referred to the CA current measured with only PBS using ERGO6 electrode, while the next four cycles showed current response of 70 nA after the addition of 1 ppm of As^{3+}. Electrochemical oxidation of As^{3+} into As^{5+} at ERGO6 electrode was confirmed by ion chromatography (IC). A solution of As^{3+} was subjected to 50 CV cycles (Figure S6b) using ERGO6 electrode and the resulting solution was used for IC measurements. This electrochemically reacted As^{3+} solution and standard As^{5+} solution showed ionic conductivity at the same retention time (Figure 3b). Interaction of As^{3+} with ERGO6 through adsorption was determined by scan rate (υ) dependent CV with 200 ppb As^{3+} (Figure S7a). Linear oxidation peak current as a function of square root υ (Figure S7c) indicated that the adsorption of As^{3+} took place onto the active sites of ERGO through a diffusion-controlled process. These surface adsorbed species were oxidized upon application of an external potential, with the response being linear with concentration of As^{3+} (Figure S7d).

To determine the limit of detection (LOD) of As^{3+} by ERGO6 electrode, we performed CA measurements at various As^{3+} concentrations (starting from 200 to 5 ppb) in PBS (Figure 3c). The experiment was repeated thrice using the

https://doi.org/10.1021/acsanm.2c02860
ACS Appl. Nano Mater. 2022, 5, 11876−11888

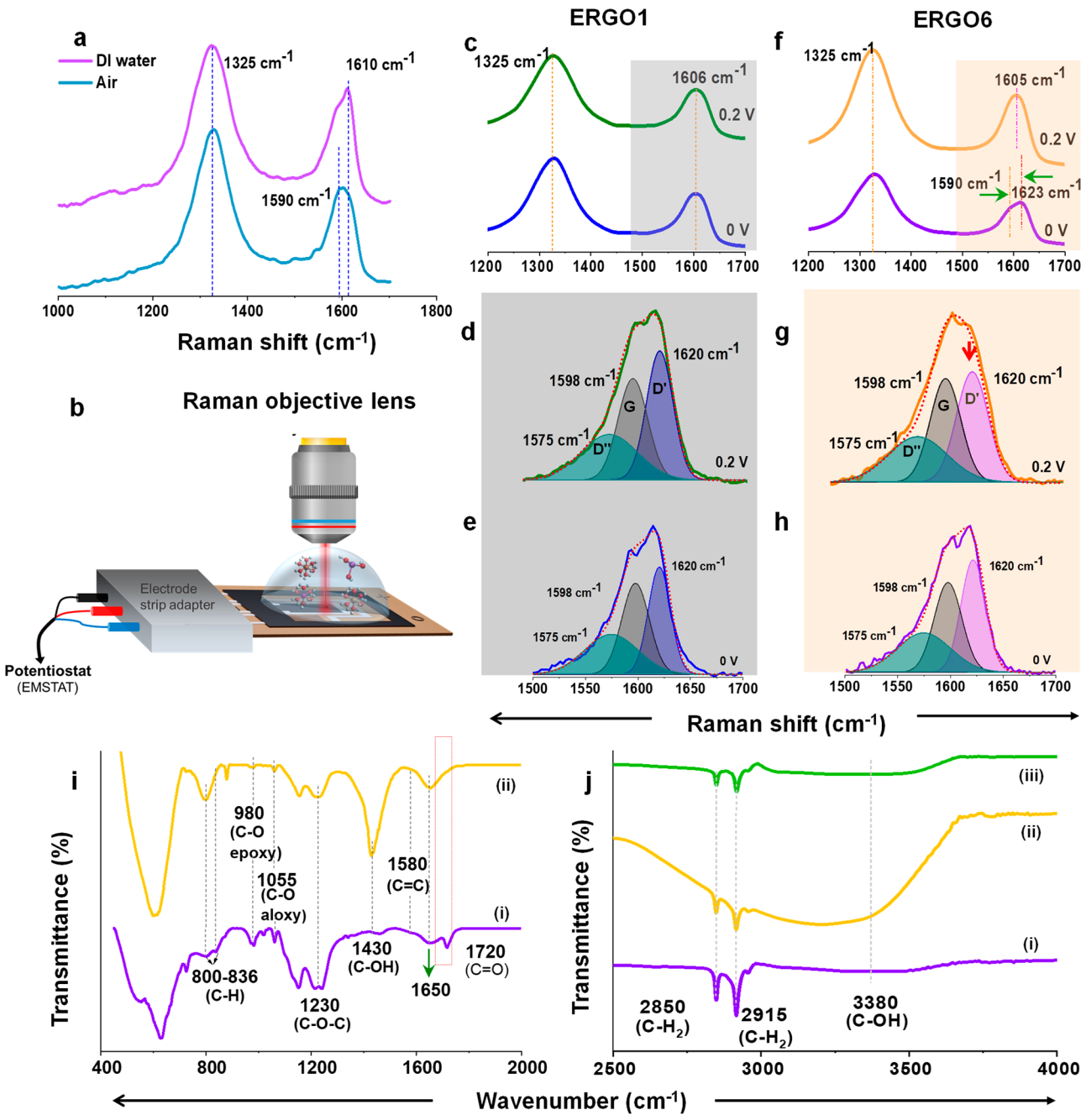

Figure 4. (a) Raman spectra of ERGO6 without (air) and with DI water. (b) Schematic depicts spectro-electrochemical (SPEC) measurement setup. During SPEC measurements, the Raman objective was focused at the surface of ERGO6 strips with and without As^{3+}-containing DI water on it and a DC potential of 0.2 V was applied to the electrode. (c) Raman spectra of ERGO1 in the presence of As^{3+} without and with the application of potential (+ 0.2 V). Gaussian peak fitting was performed on the G bands of Raman spectra of ERGO1 (d) with and (e) without the application of potential. (f) Raman spectra of ERGO6 in the presence of As^{3+} without and with application of +0.2 V. Gaussian peak fitting was performed on the G bands of the Raman spectra of ERGO6 (g) with and (h) without the application of potential. Decrease in the intensity of D′ is marked with a downward arrow. FTIR spectra of ERGO6 (i) without (purple trace) and with As^{3+} (yellow trace), (j) FTIR spectra of the same strip without As^{3+} (purple trace), with As^{3+} (yellow trace), and after electrochemical oxidation (green trace) to show the changes in OH deformation peak at higher wavenumber.

same ERGO6 strip. We further calculated statistical average of three sets of measured current, for each concentration of As^{3+}, and plotted them as a function of As^{3+} concentration (Figure 3d). The limit of detection (LOD) was up to 10 ppb within a standard deviation of 5% and the experiment was highly reproducible for multiple strips. CV was performed to check As^{3+} response of ERGO6 in field water samples (spiked with 1 ppm As^{3+}) and the response was observed at a different potential (+0.18 V). The corresponding voltammogram is shown in Figure S8a. Figure S8b represents a linear variation in response current with different As^{3+} dosages spiked into the same field water and it was recognized that LOD of As^{3+} in field water was close to 15 ppb.

Selectivity. The ability of ERGO6 to selectively detect As^{3+} was evaluated by performing CA in the presence of four potentially interfering metal ions (As^{5+}, Cu^{2+}, Fe^{2+}, and Mn^{2+}),

https://doi.org/10.1021/acsanm.2c02860
ACS Appl. Nano Mater. 2022, 5, 11876−11888

as these are seen along with As^{3+} commonly in nature. The measurement was carried out at +0.1 V with 200 ppb of As^{3+} in PBS. Individual concentrations of these interfering ions were kept 5 times higher (1 ppm). Current response was observed only with As^{3+} (Figure 3e), confirming the high specificity of ERGO6 toward As^{3+}. Selective As^{3+} response exhibited by ERGO6 electrode was also tested by measuring CV in the presence of cations (As^{5+}, Fe^{2+}, Cu^{2+}, Mn^{2+}, Ca^{2+}, Na^{+}, K^{+}, and Mg^{+}) and anions (SO_4^{2-}, NO_3^{-}, Cl^{-}, and F^{-}) common in field conditions and the potential window was kept fixed between −0.4 to +0.4 V for all ions. No peak was observed in the voltammograms for either of these ions (Figure S9), establishing the electrochemical inertness of ERGO6 to the aforementioned ions within this potential window. However, the presence of Cl^{-} in water passivates the electrode surface, which caused the oxidation potential of As^{3+} to shift to a higher value (+0.18 V). Moreover, this Cl^{-} passivation reduced the response current of 1 ppm As^{3+} (from 70 to 60 nA) in field water.

Ionic Conductivity. Having established that ERGO6 is highly sensitive and selective to As^{3+}, we set out to explore the effect of ionic conductivity on the sensitivity. In the first set of experiments, PBS solutions of different conductivities prepared in Milli-Q water were used as electrolytes during CA measurements (Figure 3f). Three sets of CA scans were carried out for each of the PBS solutions spiked with 1 ppm of As^{3+}. It was observed that As^{3+} response was independent of ionic conductivity of the electrolyte solution (within 5% of standard deviation).

In the second set of experiments, we carried out CA measurements with field water samples having different conductivity and TDS (total dissolved solids) levels, keeping the real-world application of our electrode in mind. The amplitude of the ionic current response for all these field samples was similar (Figure S10). Arsenic response of ERGO6 strip was also tested in the field water samples by spiking these with 1 ppm As^{3+}. It was noticed that the current responses for 1 ppm As^{3+} in these different field samples were close to that in PBS. As the As^{3+} response of ERGO6 electrodes remain practically unaffected by TDS and the conductivity of the field samples, these are suitable for CA-based As^{3+} sensing.

Spectroscopic understanding of the interaction of ERGO with As^{3+}. *Raman measurements.* Electrochemical measurements indicated that specific interactions drive the selective binding of As^{3+} with the ERGO surface when it was exposed to As^{3+}-contaminated water in the presence of different ions. We used Raman spectroscopy to understand the As^{3+} interaction with in-plane (sp^2) and out-of-plane (sp^3) carbons of ERGO. Raman spectra of pristine a ERGO6 electrode (Figure 4a) in air (cyan trace) exhibited two characteristic features at 1325 (D band) and 1590 cm^{-1} (G band). The origin of D and G bands is well established in the literature.[38,39] In brief, the D band originated from the structural imperfections due to the existence of large number of functional groups (hydroxyl and epoxides) on the basal plane of sp^2 carbon, while the G band was due to first-order scattering of the E_{2g} vibrational mode of sp^2-bonded carbon atoms. The Raman intensity of the D band was slightly higher than that of the G band, resulting from the sp^3-hybridized bonds. In the presence of DI water (purple trace), the G band was shifted to a higher wavenumber (1610 cm^{-1}) due to the spectral overlap of G band of ERGO with the bending mode of H−OH (1635 cm^{-1}) of adsorbed water. To confirm this, we performed Z-scan-dependent confocal Raman spectroscopy measurement in the presence of DI water from an ERGO6 electrode (Figure S11). At Z = 0, the Raman objective was focused on the surface of ERGO6, while at highest Z (Z = 400 μm), the objective was focused at bulk DI water. When Z was increased, the signal became weak and the G band shifted to a higher wavenumber. At maximum Z, both D and G bands diminished and the bending mode of H−OH appeared at 1635 cm^{-1}.

The G band of ERGO6 electrode (with and without DI water) was deconvoluted and fitted to be composed of three Gaussian peaks (Figure S12). Among these three fitted peaks, the first peak (D′′) at 1572 cm^{-1} corresponds to the amorphous phase of carbon.[39] The second peak (G), positioned at 1590 cm^{-1}, is due to the in-plane vibration of sp^2 carbon (C═C). The third peak (D′, at 1620 cm^{-1}) is associated with structural defects or the presence of sp^2 clusters/smaller sheets (as seen in the FESEM images) in the basal plane of ERGO.[40,41]

To probe As^{3+} binding to the electrode surface and its subsequent oxidation upon application of DC potential in situ, we designed a spectro-electrochemical (SPEC) measurement. Figure 4b represents a schematic illustration of the SPEC measurement setup. The objective lens of the Raman microscope was focused on the electrode to monitor the spectroscopic changes. Raman spectra were collected from ERGO1 and ERGO6 in the presence of As^{3+}-contaminated water for a comparative study, with and without an externally applied DC potential (oxidation potential of As^{3+}). Application of potential did not show any spectral changes in the presence of DI water for either of these electrodes (Figure S13). Spectral changes were not observed even in the presence of As^{3+}-contaminated water for ERGO1, before and after application of potential (Figure 4c). The fitted peaks of the G band remained unchanged in their shape and intensity (Figure 4d, e). No change in current in the CA profile (red trace, Figure S14) during SPEC measurement was observed as well. These indicated that As^{3+} did not oxidize at the surface of ERGO1. On the other hand, changes in the G band could be clearly observed for ERGO6, after application of potential (Figure 4f). Analysis of deconvoluted peaks of G band showed a decrease in the intensity of D′ (marked with a downward arrow) peak upon application of potential (Figure 4g, h). Some of the sp^2 carbon atoms at the edges of nanosheets of ERGO6 gain partial sp^3 character due to adsorption of As^{3+}. Upon application of potential, this bound As^{3+} was released into the solution as As^{5+} and the said C atoms gain their sp^2 character back, resulting in a decrease in the intensity of D′ peak. This was concurrent with an increase in CA current (green trace, Figure S14). ERGO6 electrode was washed with DI water and SPEC measurements were repeated with the same electrode to ensure the reproducibility.

This confirmed that active sites of the electrode surface were regenerated after electrochemical sensing measurements. Furthermore, ERGO6 electrode showed excellent stability (Figure S15), and the As^{3+} response did not deteriorate at high temperature (50 °C) and high humidity (80% RH) conditions.

We carried out further SPEC experiments to check for spectral changes at different potentials (from 0 to +0.5 V) and found that the intensity of the D′ peak was reduced only at +0.2 V (Figure S16). Changes in the SPEC features of an ERGO6 electrode was also explored for a few interfering ions (Cu^{2+}, As^{5+}, Fe^{3+}, Mn^{2+}). Spectral changes were not observed

https://doi.org/10.1021/acsanm.2c02860
ACS Appl. Nano Mater. 2022, 5, 11876−11888

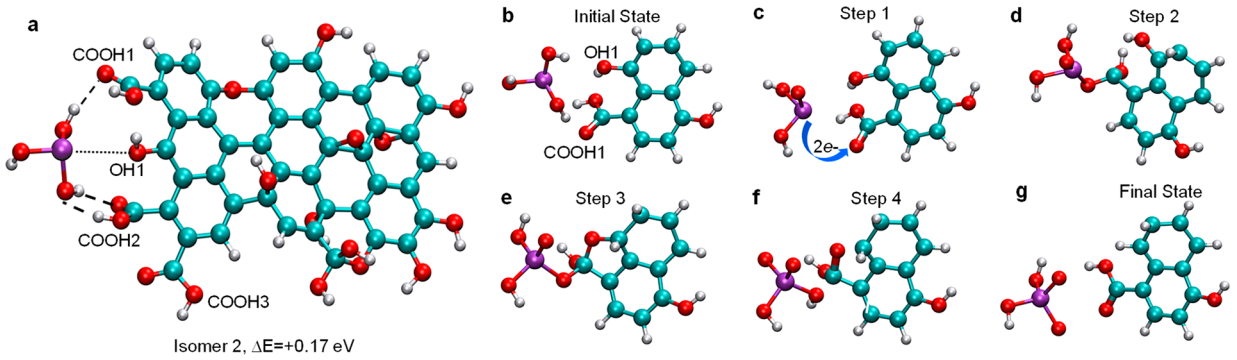

Figure 5. Suggested mechanism for oxidation of $As(OH)_3$ by interaction with the COOH1 and OH1 groups of ERGO. The initial configuration is shown as (a) the structure of isomer 2 and (b) a close-up view of isomer 2 at the active sites COOH1 and OH1. The steps of the mechanism are shown at the active sites in c−g, with the four steps being (c) approach of arsenite $As(OH)_3$, its deprotonation (to the solvent) to form $H_2AsO_3^{1-}$ and electron transfer to ERGO (step 1); (d) covalent binding (step 2) to the C(COOH1) site, which is converted from sp^2 to an unsaturated sp^3 bonding configuration; (e) regeneration intermediate formed by binding of O from an OH edge group to the C(COOH1) site (step 3); (f) detachment of $H_2AsO_4^{1-}$ and reconversion of sp^3 to sp^2 C(COOH1) as C−O is converted to C═O (step 4), with (g) replanarization and reorientation of the COOH group and the conversion of the edge COH group to CH in the final step. In the close-up views in b−g, only the atoms in the active region are shown based on a cutout cluster model of the initial configuration of isomer 2, and the viewing direction has been inverted for clarity. All structures have been optimized using the Universal Force Field. The color scheme followed for the atomic spheres is red for O, cyan for C, white for H, and purple for arsenic.[51]

for any of these individual interfering ions, while a response for As^{3+} could be detected even from a solution containing all (Figure S17).

FTIR Measurements. To identify the specific binding sites (arrangement of functional groups) of ERGO6 responsible for its exclusive attachment with As^{3+}, FTIR measurements with and without As^{3+} were carried out. Characteristic bands related to C−O (epoxy at 950 cm^{-1}), C−O (alkoxy at 1055 cm^{-1}), C−O−C (at 1230 cm^{-1}), and C−OH (at 1430 cm^{-1}) present along with carboxylic acid and carbonyl moieties on ERGO sheets (Figure 4i). The stretching vibration of C═O at 1720 cm^{-1}, the C−O (epoxy) stretching vibration at 980 cm^{-1}, and the C−O (alkoxy) stretching peak at 1055 cm^{-1} were observed.[42,43] A shoulder peak was noticed at 1580 cm^{-1}, associated with the asymmetric stretching of sp^2 hybridized C═C.[44] The out-of-plane OH bending frequency occurred at ∼600 cm^{-1}, while an O−H deformation peak was seen at ∼1430 cm^{-1}. The vibrational features at 2850 and 2915 cm^{-1} are due to the asymmetric and symmetric CH_2 stretching of ERGO, respectively (Figure 4j).

Upon As^{3+} [$As(OH)_3$] binding, two prominent spectral changes were noticed. An increase in the intensity of O−H deformation peak and OH bending mode was observed. Second, the stretching frequency of C═O at 1720 cm^{-1} diminished selectively (Figure 4i). Enhancement in the intensity of OH stretching frequency of ERGO6 at ∼3380 cm^{-1} was also evident upon As^{3+} exposure and reverted back upon application of potential (Figure 4j). To ascertain that the As^{3+} ions were chemically bound onto the ERGO surface, we collected IR spectra from an ERGO6 electrode in steps: (i) pristine electrode, (ii) treatment with As^{3+} solution and drying, (iii) thorough washing with DI water and drying, and (iv) after electrochemical CA measurement at 0.2 V (Figure S18a). Disappearance of the peak at 1720 cm^{-1} upon exposure points to interaction of the As^{3+} species to the COOH group and conversion of C═O bond into a single bond. This was explored through DFT calculation (discussed later). Vigorous washing of the strip with DI water did not bring peak at 1720 cm^{-1} back, confirming As^{3+} ions were chemically bound to the surface of ERGO. Electrochemical oxidation at +0.2 V, do, however, brought the peak at 1720 cm^{-1} back and the IR spectrum resembles that of pristine ERGO6. The electrode was regenerated at this step as oxidized species ($HAsO_4^{1-}$) was released into the solution. Disappearance of the C═O peak was not observed upon interaction of other interfering ions with the ERGO6 electrode (mixture of As^{5+}, Cu^{2+}, Fe^{2+}, Mn^{2+}). In the presence of As^{3+} along with the interfering ions, C═O peak disappeared while the signal corresponding to C−OH became prominent (Figure S18b). However, ERGO1 did not exhibit similar spectral changes upon exposure to As^{3+} (Figure S18c).

Understanding of Molecular Interactions between As^{3+} and ERGO from DFT Calculations. Binding of As^{3+} and other analyte species in the proximity of the ERGO electrode along with the oxidation mechanism of As^{3+} was investigated by density-functional theory (DFT) calculations. Details of our computational methodology can be found in Figures S21−S23. We first studied the binding of neutral $As(OH)_3$ species as this was indicated by the Pourbaix diagram to be the prevalent species, at pH ∼7. Similar binding configurations for other arsenite species such the negative ion $H_2AsO_3^-$ are expected, as their structures are very similar. In addition to isotropic noncovalent interactions such as van der Waals binding and Coulombic interactions, directional noncovalent interactions such as hydrogen bonding and weak As^+−OH^- interactions were primarily responsible for the binding and orientation of the arsenite molecule to the epoxide, COOH, and OH groups of ERGO. We obtained six lowest-energy isomers, isomers 1 to 6, for the arsenite-ERGO adduct from our DFT geometry optimizations, where binding occurs at different sites of ERGO and these geometries can be visualized in Figure S22. The details of the binding site, number and type of bonding interaction, and bonding distances, as well as their total and relative energies with respect to the lowest energy isomer 1, are provided in Table S4. We found that the most stable isomer 1 was at the surface position with $As(OH)_3$ making two hydrogen bonds, one to an epoxide group (EP1) O atom and the other to an O atom of a surface OH group (OH2), marked with dashed lines. A third, but weaker interaction occurs between the electropositive As

https://doi.org/10.1021/acsanm.2c02860
ACS Appl. Nano Mater. 2022, 5, 11876−11888

atom and an O atom of another surface OH group of ERGO (dotted line). The bond lengths of the hydrogen bonds were 1.91 Å with the hydroxyl group (OH2), 1.88 Å with the epoxide group (EP1), and that of the $As^{+}-OH^{-}$ (OH4) interaction at 2.55 Å. In addition, the delocalized π-electron system of graphenic areas of the ERGO surface strongly interact through an electrostatic attraction with the partially positive As atom, increasing the binding strength at the surface position. Our lowest-energy isomer binding site at the surface agrees with the study of Reynosa-Martinez et al.,[45] in which the graphenic-surface site binding energy was found to be the lowest, followed by edge or surface hydroxyl and epoxide groups, although COOH groups were not considered in their models.

The next-lowest-energy isomer has $As(OH)_3$ near an OH group (OH1) sandwiched between two neighboring COOH groups, COOH1 and COOH2, in an edge position (Figure 5a and Figure S22b). The relative energy to the lowest isomer is 0.17 eV and binding occurs via three hydrogen bonds to the COOH1 and COOH2 groups (dashed lines) and an $As^{+}-OH^{-}$ interaction with the OH1 (dotted line), with bond lengths shown in Table S4. Isomer 3, with relative energy of 0.21 eV, the $As(OH)_3$ is bonded by two hydrogen bonds to the COOH1 group. Isomers 4 and 5, possess higher relative-energy (0.4−0.5 eV) and involve only one hydrogen bond between $As(OH)_3$ and COOH1 group, and an edge lactone (COC1) group, respectively. Lastly, isomer 6 involves only a weak $As^{+}-OH^{-}$ interaction with an edge hydroxyl (OH7) group, without any hydrogen bonding with higher relative energy of 0.65 eV compared to isomer 1. The stability of the ERGO-$As(OH)_3$ isomers in the edge position was found to increase with the number of hydrogen bonding interactions with COOH (see Table S4) and weak $As^{+}-OH^{-}$ interactions. From our starting configurations for isomers 1 to 6, after local minimization of the potential energy surface, we found only noncovalent binding modes of arsenite are accessible in our calculations. However, direct covalent binding of arsenic to oxygen has been observed experimentally in the interaction of arsenite [$As(OH)_3$] with the COOH and OH functional groups present in natural organic matter (NOM) by X-ray absorption fine structure spectroscopy. Presence of As−O−C bond, forming between arsenite and the oxygen atoms in the functional groups, was seen. This binding is thought to occur via a ligand-exchange reaction involving the displacement of one of the arsenite OH ligands into the aqueous solvent by the ketone or hydroxyl group O atom, hence, the As center remains triply coordinated with O atoms.[46] Since the COOH and OH functional groups of NOM are also found in ERGO, it is possible that covalent binding of arsenite to the COOH group of ERGO could also occur, as shown in the structure presented in Figure S21, which we also verified to be stable using DFT. The stability of As−O(COOH) bonding and its identification in NOM, which has similar functional groups to ERGO, supports the possibility of As covalently binding to a ketone O atom during the oxidation mechanism.

Our experiments also show that the arsenite oxidation mechanism involves structural changes (IR spectrum) and preferably occurs at COOH sites with some binding to OH groups. Since the binding of $As(OH)_3$ preferentially occurs at ERGO surface sites, and the second site preference is at the edge sites with COOH moieties, the question arises as to why the less energetically favorable edge sites are preferred for oxidation. Surface epoxide and hydroxyl groups are associated with higher energy barriers which would arise in the mechanism during the covalent binding of the epoxide or hydroxyl O atom to arsenite to form and its subsequent detachment to form arsenate. Higher energy barriers are associated with the detachment of oxygen atoms from ERGO surface-bonded OH and epoxide functional groups, as these are both strongly covalently bonded to the carbon atoms and are subject to stronger noncovalent interactions with the graphenic surface of ERGO. A further energy barrier that may exist during the release of As^{5+} species into the solution from the surface of ERGO is due to the stronger electrostatic and van der Waals interactions of As^{5+} species with the surface and any steric hindrance from the stacked sheets of ERGO. On the other hand, one would expect much lower energy barriers in mechanistic pathways involving the edge sites. Our proposed mechanism involves the oxidation of arsenite by the ketone oxygen which cleaves to form the arsenate species.

We may conceive the oxidation mechanism to be occurring in four stages: (1) approach of As^{3+} to edge functional groups of ERGO, (2) covalent binding interaction of As with a ketone O atom and formation of the four-coordinated As metastable intermediate, (3) regeneration of COOH by binding of a nearby hydroxyl O atom to a COOH carbon atom, and (4) detachment of As^{5+} from ERGO and release into the solution. A possible mechanistic pathway beginning from an edge site configuration of COOH1 and OH1 of isomer 2 is depicted in the active site region (Figure 5b-5g). The conversion of As^{3+} to As^{5+} involves the binding of an additional O atom to As which originates from the electron-rich nucleophilic ketone on the edges of graphene oxide. After a $2e^{-}$ electron transfer from As^{3+} in the vicinity of a COOH group, as shown in Figure 5c, highly electropositive As atom would be strongly electrostatically attracted to the electrons of the lone-pair O 2p orbitals and electron-rich double bond of the ketone O atom. This would facilitate the reorientation of the As^{5+} intermediate and the formation of an As−O (ketone) covalent bond to form the four-coordinated As center as shown in step 2 in Figure 5d. In step 3, the carbon atom of the COOH group would be converted to sp^3 and a neighboring hydroxyl oxygen would bind as a C(COOH)−O−C(OH) bridge, as seen in Figure 5e. In step 4, the H_2AsO_4 structural unit would detach with the former ketone O atom, and would be released into the solution as $H_2AsO_4^{-}$, leaving the COOH group intact and with the loss of an O atom from an edge hydroxyl group from ERGO (Figure 5f, g). The mechanism described is consistent with the changes observed in the IR spectra at the COOH and OH functional groups and the overall reaction is a transfer of an O atom from ERGO to As^{3+} to form As^{5+}, and a transfer of $2e^{-}$ from As^{3+} to ERGO. The same mechanism with the entire GO sheet is presented in Figure S28. In the case of the structure shown in Figure S23, where $As(OH)_3$ is initially covalently bonded to a COOH or OH group, a similar mechanism may also occur but it would begin at step 2 (Figure 5c).

The mechanism proposed depends on the proximity of the COOH and OH group, and several studies indicate that there is a tendency for clustering of functional groups, or oxygen atoms, in rGO or ERGO which supports the mechanism.[47] In the case that the COOH group is more isolated, a slightly more distant OH group may migrate by diffusive site-to-site hopping along either from the edges or surface of ERGO, by a thermal and potential-driven process,[48,49] to regenerate the COOH group in the final step of the mechanism.[50] In the absence of nearby COOH and OH groups, the regeneration of COOH

https://doi.org/10.1021/acsanm.2c02860
ACS Appl. Nano Mater. 2022, 5, 11876−11888

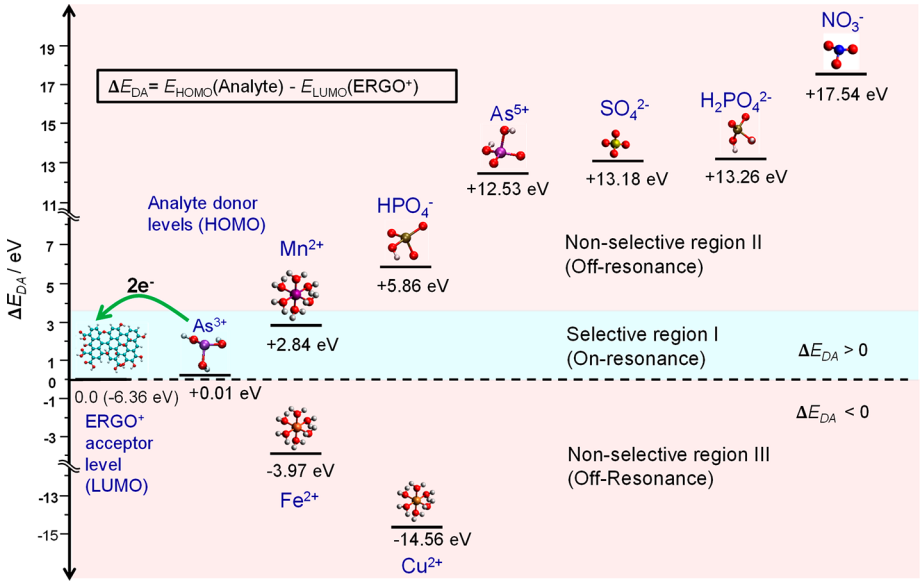

Figure 6. Donor–acceptor energy-level difference diagram for the ERGO LUMO acceptor level and the analyte ions' HOMO donor levels computed using DFT. The value of the donor–acceptor energy-level difference, $\Delta E_{DA} = E_{HOMO}(\text{Analyte}) - E_{LUMO}(\text{ERGO}(6))^+$ is shown below the energy level for each ion. Lower positive values of ΔE_{DA} indicate higher selectivity, hence, the unique sensitivity and selectivity toward As^{3+} with ΔE_{DA} = 0.01 eV. The donor analyte levels of As and Mn lie in the selectivity window of ΔE_{DA} of 0 to 3 eV, in which resonant charge transport occurs from these analyte ions to ERGO, and is shown by the central blue-shaded region. The other analyte anions and cation donor levels lie in the nonselective region (red-shaded background) having larger and negative values of ΔE_{DA}, respectively. The color scheme followed for the atomic spheres is red for O, cyan for C, white for H, purple for As, magenta for Mn, orange for Fe, gold for Cu, brown for P, yellow for S, and blue for N.

group may not be possible and the bound As^{3+} species may detach from the O atom of the COOH group and recover its original structural and electronic configuration in the solution in order to stabilize the COOH group.

The binding of other analyte species to ERGO, COOH groups of isomer 2 was tested and several analytes (Fe^{2+}, Cu^{2+}, Mn^{2+}, As^{5+}, SO_4^{2-}, HPO_4^-, $H_2PO_4^{2-}$, NO_3^-, etc.) were found to be able to bind as strongly as arsenite using hydrogen bonding (see optimized structures in Figures S24 to S27 and binding energies in Table S5). Hence, the ion selectivity cannot be explained based on differences in the binding energies of different analytes to ERGO. The compact XY_3 pyramidal shape and three-coordinated As center of arsenite make it sterically more feasible, compared to the other ions, which have higher coordination numbers of four or more (apart from nitrate), to engage in inner-sphere bonding with O atoms of COOH groups. We probed the ion-selectivity mechanism occurring via electron transfer from analyte ions to ERGO, by conducting an energy-level analysis of ERGO and analyte ions based on DFT calculations of the frontier-orbital energies. The details of our method are given in section S22. According to electron-transfer theory, electron transfer occurs from the HOMO of the donor analyte molecule, when it is above the LUMO of the acceptor, $ERGO^+$. However, in biomolecules such as proteins and enzymes, such as the biomimicking arsenic oxidase (AiO) enzyme, electron transfer generally occurs over longer ranges, and may be attributed to a tunneling electron transfer process, which is equivalently known as "on-resonance" charge transfer.[52] Similar resonant charge-transfer processes are also found to occur in molecular junctions when the electrode and frontier orbitals are aligned.[53]

Similarly, in the initial steps of the mechanism, the ERGO electrode would be involved in noncovalent binding interactions with the analyte, and hence a similar tunneling electron transport process may be expected to occur from the solvated analyte species, when they are within a range of ~0.5 nm, or weakly bound to the ERGO electrode, which leads to the binding of the analyte in an intermediate step.

Subsequently, as already described in our suggested mechanism, inner-sphere structural changes involving the oxidation of the molecular analyte and the further reduction of the ERGO may occur.

In resonant charge transfer processes, the alignment and proximity of the donor and acceptor levels is the main criterion for charge transfer to occur by tunneling, and the degree of alignment is given by energy difference, between the donor level and the acceptor level, $\Delta E_{DA} = E_{HOMO}(\text{Analyte}) - E_{LUMO}(\text{ERGO}^+)$. For close energy levels, termed "on-resonance", corresponding to smaller values of ΔE_{DA}, resonant tunneling will lead to enhanced electron transport kinetics. The energy-level diagram of relative positions of donor levels of the analyte ions and acceptor level $ERGO^+$ model is shown in Figure 6 and the values are tabulated in Table S7. The values of ΔE_{DA} computed using DFT, show that the As^{3+} (ΔE_{DA} = 0.01 eV) and Mn^{2+} (ΔE_{DA} = 2.84 eV) ions are found to lie closer and just above the acceptor level of ERGO compared with all the other cations and ions. This suggests that ion-selectivity mechanism is mediated by the occurrence resonant charge-transport which leads to the electron transfer which initiates the oxidation mechanism, when donor and acceptor levels are close in energy with a small ΔE_{DA}, or "on-resonance". We may define an ion-selectivity window based on the observed correspondence between selectivity indicate by the calculations and experimental results, as the energy region, $0 < \Delta E_{DA} < 3$ eV, indicated by the central blue shaded band in Figure 6 encloses the levels of As^{3+} and Mn^{2+}.[54] It is seen in Figure 6 that donor HOMO energy levels of all the other analyte ions, which are not found to be selective in experiment, also lie outside the selectivity window in the nonselective

https://doi.org/10.1021/acsanm.2c02860
ACS Appl. Nano Mater. 2022, 5, 11876–11888

region indicated by red shading in Figure 6, corresponding to ΔE_{DA} either less than zero or above 3 eV. This nonselective region where HOMO levels of the analyte ions are further away in energy from the LUMO of $ERGO^+$ and are "off-resonance" so that resonant charge transport does not occur. Remarkably, out of all the analyte species considered, the HOMO donor level of arsenite, $As(OH)_3$, is found to be the closest and slightly above (ΔE_{DA} = +0.01 eV) to the LUMO acceptor level of $ERGO^+$ for all the different types of $ERGO^+$ models (rectangular sheet model 1, model 2, and hexagonal flake model 3), which explains the unique selectivity and high sensitivity of the sensor toward As^{3+}. The next closest donor level is Mn at ΔE_{DA} = 2.84 eV, which also detectable but at different potential (0.35 V), which leads to "on-resonance" electron transfer for both As^{3+} and Mn^{2+} ions, at their respective electrode potentials. Furthermore, it is seen that the HOMO levels of the Fe^{2+} and Cu^{2+} lie further below the LUMO of ERGO6$^+$ with ΔE_{DA}=-3.57 eV and −14.6 eV, respectively, and are off-resonance and also energetically unfavorable as ΔE_{DA} < 0. Finally, for the anionic species, although their donor levels lie above the $ERGO^+$ acceptor level satisfying the energetic-favorability condition (ΔE_{DA} > 0), their HOMO donor levels are in the higher-energy range, i.e., "off-resonance" with ΔE_{DA} > 5 eV) and most lie above ΔE_{DA} value of 12 eV, so resonant charge transfer does not occur. Furthermore, it is also found that when the neutral ERGO models are used, their LUMO levels are much higher at 3.71−3.51 eV and further away from the arsenite HOMO level (see Table S6), hence, the positive surface charge density of ERGO6 is also a necessary factor in the selectivity and electron transfer mechanism. Thus, the high selectivity and sensitivity to As^{3+}, and also to Mn^{2+} at a different potential, and also the nonselectivity to Fe^{2+}, Cu^{2+}, HPO_4^-, As^{5+}, $H_2PO_4^{2-}$, SO_4^{2-}, and NO_3^-, is attributed to a resonant charge transfer effect similar to that found in molecular junctions and bionanoelectronic systems.

CONCLUSION

Electrochemically reduced graphene oxide (ERGO) with modified electronic properties and functionalities prepared through controlled electro-reduction of its functional groups exhibits highly sensitive and selective As^{3+} sensing in water samples down to 10 ppb. The chronoamperometric response of ERGO with As^{3+} was independent of the ionic conductivity of the electrolyte. The biomimicking activity of the electrode was manifested through several analytical and spectroscopy measurements. Spectroelectrochemical measurements confirmed that sensing mechanism of As^{3+} involved two processes: selective adsorption of As^{3+} by the acid functional groups of ERGO and the subsequent electro-oxidation of As^{3+} ion on the surface of ERGO upon application of a potential. The compact pyramidal shape of As^{3+} and the possibility of forming a four-coordinated As^{5+} species make it a more suitable candidate among various analytes to undergo oxidation with concomitant structural changes at an ERGO COOH functional group. DFT calculations showed that noncovalent directional hydrogen bonding and weaker As^+-O^- interactions are involved in the initial mechanistic steps of binding of As^{3+} ions to ERGO, prior to electron transfer and binding to the ketone O atom of the COOH group. Subsequently, As^{5+} species are formed, which are released into the solution with regeneration of the COOH group, by the addition of oxygen atoms from the neighboring OH functional groups. The origin of unique selectivity and sensitivity of the sensor toward As^{3+} was understood by an energy-level correlation analysis of the analyte species and models of ERGO. The computed energy-level diagram showed an almost perfect matching of the donor HOMO level of As^{3+} and the LUMO acceptor level of the positively charged ERGO model, which is not the case for any of the other analyte ions considered. Based on this, a resonant charge-transfer mechanism is proposed to explain the selectivity, similar to that found in electronic transport in bionanoelectronic systems and molecular junctions. Thus, the surface of ERGO exhibits enzyme-like selective sensing mechanism for As^{3+}, similar to the arsenite oxidase enzyme. Hence, this electrode can be a potential candidate for arsenic sensing with excellent selectivity and sensitivity.

ASSOCIATED CONTENT

Supporting Information

The Supporting Information is available free of charge at https://pubs.acs.org/doi/10.1021/acsanm.2c02860.

Details of characterizations including FESEM-EDX analysis, XPS, EIS fitting parameters, and calculation of dielectric constant, As^{3+} concentration-dependent response of ERGO6 and selectivity study, As^{3+} in field water, spectroelectrochemistry analysis with and without As^{3+} for both ERGO1 and ERGO6, ion chromatography analysis, FTIR analysis of ERGO1 and ERGO6, coordinates of ERGO models and ERGO-analyte adduct structures, and the structures involved in the steps of the oxidation mechanism (PDF)

AUTHOR INFORMATION

Corresponding Author

Thalappil Pradeep − *HSB 148, Unit of Nanoscience, Department of Chemistry, Indian Institute of Technology Madras, Chennai 600036, India;* orcid.org/0000-0003-3174-534X; Email: pradeep@iitm.ac.in

Authors

Sourav Kanti Jana − *HSB 148, Unit of Nanoscience, Department of Chemistry, Indian Institute of Technology Madras, Chennai 600036, India;* orcid.org/0000-0001-5772-7022

Kamalesh Chaudhari − *HSB 148, Unit of Nanoscience, Department of Chemistry, Indian Institute of Technology Madras, Chennai 600036, India; International Centre for Clean Water, Chennai, Tamil Nadu 600113, India*

Md Rabiul Islam − *HSB 148, Unit of Nanoscience, Department of Chemistry, Indian Institute of Technology Madras, Chennai 600036, India*

Ganapati Natarajan − *International Centre for Clean Water, Chennai, Tamil Nadu 600113, India*

Tripti Ahuja − *HSB 148, Unit of Nanoscience, Department of Chemistry, Indian Institute of Technology Madras, Chennai 600036, India*

Anirban Som − *HSB 148, Unit of Nanoscience, Department of Chemistry, Indian Institute of Technology Madras, Chennai 600036, India;* orcid.org/0000-0002-6646-679X

Ganesan Paramasivam − *HSB 148, Unit of Nanoscience, Department of Chemistry, Indian Institute of Technology Madras, Chennai 600036, India*

Addanki Raghavendra − *National Institute of Technology Calicut, Kattangal, Kerala 673601, India; International*

Centre for Clean Water, Chennai, Tamil Nadu 600113, India

Chennu Sudhakar − *HSB 148, Unit of Nanoscience, Department of Chemistry, Indian Institute of Technology Madras, Chennai 600036, India*

Complete contact information is available at: https://pubs.acs.org/10.1021/acsanm.2c02860

Author Contributions

†S.K.J. and K.C. contributed equally to this work. S.K.J. planned and designed the whole project. He fabricated the electrodes and performed characterization and optimization of those. K.C. helped during sensing measurements and analyzed the sensing data. R.I. prepared GO samples and helped to carry out IR measurements. G.N. designed and supervised the computational study and carried out the calculations. A.S. helped in editing the manuscript. P.G. performed all-electron DFT optimizations of the arsenite-ERGO adducts. A.R. created additional sheet and hexagonal flake models of ERGO, carried out force-field calculations of the oxidation mechanism, and contributed to the production of figures. T.A. and C.S. helped to carry out Raman and XPS measurements, respectively. T.P. supervised the whole project..

Notes

The authors declare no competing financial interest.

■ ACKNOWLEDGMENTS

All authors are thankful to E. Sundarraj for FESEM measurements. We acknowledge the use of computing resources at HPCE, IIT Madras. R.I. thanks CSIR, Government of India, for a research fellowship. G.P. thanks IIT Madras for an Institute Post-Doctoral Fellowship. The authors thank A. Chakraborty and A. R. Kini for help in making the figures. T.A. and S.C. thank IIT Madras for their fellowships. A.R. thanks the International Centre for Clean Water for an internship. T.P. thanks the Department of Science and Technology, Government of India, for research funding.

■ ABBREVIATIONS

GO, graphene oxide; ERGO, electrochemically reduced graphene oxide; CV, cyclic voltammetry; CA, chronoamperometry; DFT, density functional theory

■ REFERENCES

(1) Nagar, A.; Pradeep, T. Clean Water through Nanotechnology: Needs, Gaps, and Fulfillment. *ACS Nano* **2020**, *14* (6), 6420−6435.
(2) Sabir, F.; Zeeshan, M.; Laraib, U.; Barani, M.; Rahdar, A.; Cucchiarini, M.; Pandey, S. DNA Based and Stimuli-Responsive Smart Nanocarrier for Diagnosis and Treatment of Cancer: Applications and Challenges. *Cancers* **2021**, *13* (14), 3396.
(3) Barani, M.; Mukhtar, M.; Rahdar, A.; Sargazi, S.; Pandey, S.; Kang, M. Recent Advances in Nanotechnology-Based Diagnosis and Treatments of Human Osteosarcoma. *Biosensors* **2021**, *11* (2), 55.
(4) Sargazi, S.; Mukhtar, M.; Rahdar, A.; Bilal, M.; Barani, M.; Díez-Pascual, A. M.; Behzadmehr, R.; Pandey, S. Opportunities and Challenges of Using High-Sensitivity Nanobiosensors to Detect Long Noncoding RNAs: A Preliminary Review. *Int. J. Biol. Macromol.* **2022**, *205*, 304−315.
(5) Wei, H.; Wang, E. Nanomaterials with Enzyme-like Characteristics (Nanozymes): Next-Generation Artificial Enzymes. *Chem. Soc. Rev.* **2013**, *42* (14), 6060−6093.
(6) Lee, J. H.; Jin, H.-E.; Desai, M. S.; Ren, S.; Kim, S.; Lee, S.-W. Biomimetic Sensor Design. *Nanoscale* **2015**, *7* (44), 18379−18391.
(7) Breslow, R. Biomimetic Chemistry and Artificial Enzymes: Catalysis by Design. *Acc. Chem. Res.* **1995**, *28* (3), 146−153.
(8) Heller, A.; Feldman, B. Electrochemical Glucose Sensors and Their Applications in Diabetes Management. *Chem. Rev.* **2008**, *108* (7), 2482−2505.
(9) Male, K. B.; Hrapovic, S.; Santini, J. M.; Luong, J. H. T. Biosensor for Arsenite Using Arsenite Oxidase and Multiwalled Carbon Nanotube Modified Electrodes. *Anal. Chem.* **2007**, *79* (20), 7831−7837.
(10) Podgorski, J.; Berg, M. Global Threat of Arsenic in Groundwater. *Science* **2020**, *368* (6493), 845−850.
(11) Conrads, T.; Hemann, C.; George, G. N.; Pickering, I. J.; Prince, R. C.; Hille, R. The Active Site of Arsenite Oxidase from Alcaligenes Faecalis. *J. Am. Chem. Soc.* **2002**, *124* (38), 11276−11277.
(12) Masscheleyn, P. H.; Delaune, R. D.; Patrick, W. H. Effect of Redox Potential and PH on Arsenic Speciation and Solubility in a Contaminated Soil. *Environ. Sci. Technol.* **1991**, *25* (8), 1414−1419.
(13) Ellis, P. J.; Conrads, T.; Hille, R.; Kuhn, P. Crystal Structure of the 100 KDa Arsenite Oxidase from Alcaligenes Faecalis in Two Crystal Forms at 1.64 Å and 2.03 Å. *Structure* **2001**, *9* (2), 125−132.
(14) Duval, S.; Santini, J. M.; Nitschke, W.; Hille, R.; Schoepp-Cothenet, B. The Small Subunit AroB of Arsenite Oxidase: LESSONS ON THE [2Fe-2S] RIESKE PROTEIN SUPERFAMILY. *J. Biol. Chem.* **2010**, *285* (27), 20442−20451.
(15) Teoh, W. K.; Salleh, F. M.; Shahir, S. Characterization of Thiomonas Delicata Arsenite Oxidase Expressed in Escherichia Coli. *3 Biotech* **2017**, *7* (2), 97.
(16) Karakoti, A.; Singh, S.; Dowding, J. M.; Seal, S.; Self, W. T. Redox-Active Radical Scavenging Nanomaterials. *Chem. Soc. Rev.* **2010**, *39* (11), 4422−4432.
(17) Xie, J.; Zhang, X.; Wang, H.; Zheng, H.; Huang, Y.; Xie, J. Analytical and Environmental Applications of Nanoparticles as Enzyme Mimetics. *TrAC Trends Anal. Chem.* **2012**, *39*, 114−129.
(18) Celardo, I.; Pedersen, J. Z.; Traversa, E.; Ghibelli, L. Pharmacological Potential of Cerium Oxide Nanoparticles. *Nanoscale* **2011**, *3* (4), 1411−1420.
(19) Dai, X.; Nekrassova, O.; Hyde, M. E.; Compton, R. G. Anodic Stripping Voltammetry of Arsenic(III) Using Gold Nanoparticle-Modified Electrodes. *Anal. Chem.* **2004**, *76* (19), 5924−5929.
(20) Luong, J. H. T.; Lam, E.; Male, K. B. Recent Advances in Electrochemical Detection of Arsenic in Drinking and Ground Waters. *Anal. Methods* **2014**, *6* (16), 6157−6169.
(21) Gupte, T.; Jana, S. K.; Mohanty, J. S.; Srikrishnarka, P.; Mukherjee, S.; Ahuja, T.; Sudhakar, C.; Thomas, T.; Pradeep, T. Highly Sensitive As3+ Detection Using Electrodeposited Nanostructured MnOx and Phase Evolution of the Active Material during Sensing. *ACS Appl. Mater. Interfaces* **2019**, *11* (31), 28154−28163.
(22) Gao, C.; Yu, X.-Y.; Xiong, S.-Q.; Liu, J.-H.; Huang, X.-J. Electrochemical Detection of Arsenic(III) Completely Free from Noble Metal: Fe3O4Microspheres-Room Temperature Ionic Liquid Composite Showing Better Performance than Gold. *Anal. Chem.* **2013**, *85* (5), 2673−2680.
(23) Subramanian, V.; Lee, S.; Jena, S.; Jana, S. K.; Ray, D.; Kim, S. J.; Thalappil, P. Enhancing the Sensitivity of Point-of-Use Electrochemical Microfluidic Sensors by Ion Concentration Polarisation-A Case Study on Arsenic. *Chem. Sens. Actuators B* **2020**, *304* (18), 127340.
(24) Kempahanumakkagari, S.; Deep, A.; Kim, K.-H.; Kumar Kailasa, S.; Yoon, H.-O. Nanomaterial-Based Electrochemical Sensors for Arsenic - A Review. *Biosens. Bioelectron.* **2017**, *95*, 106−116.
(25) Wei, X.-Q.; Hao, L.-Y.; Shao, X.-R.; Zhang, Q.; Jia, X.-Q.; Zhang, Z.-R.; Lin, Y.-F.; Peng, Q. Insight into the Interaction of Graphene Oxide with Serum Proteins and the Impact of the Degree of Reduction and Concentration. *ACS Appl. Mater. Interfaces* **2015**, *7* (24), 13367−13374.
(26) Kumar, S.; Parekh, S. H. Linking Graphene-Based Material Physicochemical Properties with Molecular Adsorption, Structure and Cell Fate. *Commun. Chem.* **2020**, *3* (1), 1−11.

(27) Liu, M.; Zhao, H.; Chen, S.; Yu, H.; Quan, X. Interface Engineering Catalytic Graphene for Smart Colorimetric Biosensing. *ACS Nano* **2012**, *6* (4), 3142−3151.
(28) Song, Y.; Qu, K.; Zhao, C.; Ren, J.; Qu, X. Graphene Oxide: Intrinsic Peroxidase Catalytic Activity and Its Application to Glucose Detection. *Adv. Mater.* **2010**, *22* (19), 2206−2210.
(29) Liu, M.; Zhao, H.; Chen, S.; Yu, H.; Quan, X. Stimuli-Responsive Peroxidase Mimicking at a Smart Graphene Interface. *Chem. Commun.* **2012**, *48* (56), 7055−7057.
(30) Bolotsky, A.; Butler, D.; Dong, C.; Gerace, K.; Glavin, N. R.; Muratore, C.; Robinson, J. A.; Ebrahimi, A. Two-Dimensional Materials in Biosensing and Healthcare: From *In Vitro* Diagnostics to Optogenetics and Beyond. *ACS Nano* **2019**, *13* (9), 9781−9810.
(31) Islam, M. R.; Gupta, S. S.; Jana, S. K.; Srikrishnarka, P.; Mondal, B.; Chennu, S.; Ahuja, T.; Chakraborty, A.; Pradeep, T. A Covalently Integrated Reduced Graphene Oxide-Ion-Exchange Resin Electrode for Efficient Capacitive Deionization. *Adv. Mater. Interfaces* **2021**, *8* (5), 2001998.
(32) Tu, N. D. K.; Choi, J.; Park, C. R.; Kim, H. Remarkable Conversion Between N- and p-Type Reduced Graphene Oxide on Varying the Thermal Annealing Temperature. *Chem. Mater.* **2015**, *27* (21), 7362−7369.
(33) Tan, S.; Bélanger, D. Characterization and Transport Properties of Nafion/Polyaniline Composite Membranes. *J. Phys. Chem. B* **2005**, *109* (49), 23480−23490.
(34) Zhao, X.; Hayner, C. M.; Kung, M. C.; Kung, H. H. Flexible Holey Graphene Paper Electrodes with Enhanced Rate Capability for Energy Storage Applications. *ACS Nano* **2011**, *5* (11), 8739−8749.
(35) Jana, S. K.; Banerjee, S.; Bayan, S.; Inta, H. R.; Mahalingam, V. Rectification and Amplification of Ionic Current in Planar Graphene/Graphene-Oxide Junctions: An Electrochemical Diode and Transistor. *J. Phys. Chem. C* **2018**, *122* (21), 11378−11384.
(36) Meng, F.; Li, J.; Cushing, S. K.; Zhi, M.; Wu, N. Solar Hydrogen Generation by Nanoscale p-n Junction of p-Type Molybdenum Disulfide/n-Type Nitrogen-Doped Reduced Graphene Oxide. *J. Am. Chem. Soc.* **2013**, *135* (28), 10286−10289.
(37) Li, J.; Meng, F.; Suri, S.; Ding, W.; Huang, F.; Wu, N. Photoelectrochemical Performance Enhanced by a Nickel Oxide-Hematite p-n Junction Photoanode. *Chem. Commun.* **2012**, *48* (66), 8213−8215.
(38) Ferrari, A. C.; Basko, D. M. Raman Spectroscopy as a Versatile Tool for Studying the Properties of Graphene. *Nat. Nanotechnol.* **2013**, *8* (4), 235−246.
(39) Ferrari, A. C.; Meyer, J. C.; Scardaci, V.; Casiraghi, C.; Lazzeri, M.; Mauri, F.; Piscanec, S.; Jiang, D.; Novoselov, K. S.; Roth, S.; Geim, A. K. Raman Spectrum of Graphene and Graphene Layers. *Phys. Rev. Lett.* **2006**, *97* (18), 187401.
(40) Lopez-Diaz, D.; Lopez Holgado, M.; Garcia-Fierro, J. L.; Velazquez, M. M. Evaluation of the Raman Spectrum with the Chemical Composition of Graphene Oxide. *J. Phys. Chem. C* **2017**, *121*, 20489−20497.
(41) Eckmann, A.; Felten, A.; Mishchenko, A.; Britnell, L.; Krupke, R.; Novoselov, K. S.; Casiraghi, C. Probing the Nature of Defects in Graphene by Raman Spectroscopy. *Nano Lett.* **2012**, *12* (8), 3925−3930.
(42) Zhang, J.; Yang, H.; Shen, G.; Cheng, P.; Zhang, J.; Guo, S. Reduction of Graphene Oxide ViaL-Ascorbic Acid. *Chem. Commun.* **2010**, *46* (7), 1112−1114.
(43) Acik, M.; Mattevi, C.; Gong, C.; Lee, G.; Cho, K.; Chhowalla, M.; Chabal, Y. J. The Role of Intercalated Water in Multilayered Graphene Oxide. *ACS Nano* **2010**, *4* (10), 5861−5868.
(44) Acik, M.; Lee, G.; Mattevi, C.; Pirkle, A.; Wallace, R. M.; Chhowalla, M.; Cho, K.; Chabal, Y. The Role of Oxygen during Thermal Reduction of Graphene Oxide Studied by Infrared Absorption Spectroscopy. *J. Phys. Chem. C* **2011**, *115* (40), 19761−19781.
(45) Reynosa-Martínez, A. C.; Tovar, G. N.; Gallegos, W. R.; Rodríguez-Meléndez, H.; Torres-Cadena, R.; Mondragón-Solórzano, G.; Barroso-Flores, J.; Alvarez-Lemus, M. A.; Montalvo, V. G.; López-Honorato, E. Effect of the Degree of Oxidation of Graphene Oxide on As(III) Adsorption. *J. Hazard. Mater.* **2020**, *384*, 121440.
(46) Biswas, A.; Besold, J.; Sjöstedt, C.; Gustafsson, J. P.; Scheinost, A. C.; Planer-Friedrich, B. Complexation of Arsenite, Arsenate, and Monothioarsenate with Oxygen-Containing Functional Groups of Natural Organic Matter: An XAS Study. *Environ. Sci. Technol.* **2019**, *53* (18), 10723−10731.
(47) Mouhat, F.; Coudert, F.-X.; Bocquet, M.-L. Structure and Chemistry of Graphene Oxide in Liquid Water from First Principles. *Nat. Commun.* **2020**, *11* (1), 1566.
(48) Kumar, P. V.; Bardhan, N. M.; Chen, G.-Y.; Li, Z.; Belcher, A. M.; Grossman, J. C. New Insights into the Thermal Reduction of Graphene Oxide: Impact of Oxygen Clustering. *Carbon* **2016**, *100*, 90−98.
(49) Boukhvalov, D. W. Modeling of Hydrogen and Hydroxyl Group Migration on Graphene. *Phys. Chem. Chem. Phys.* **2010**, *12* (47), 15367.
(50) Novotny, Z.; Nguyen, M.-T.; Netzer, F. P.; Glezakou, V.-A.; Rousseau, R.; Dohnálek, Z. Formation of Supported Graphene Oxide: Evidence for Enolate Species. *J. Am. Chem. Soc.* **2018**, *140* (15), 5102−5109.
(51) Rappe, A. K.; Casewit, C. J.; Colwell, K. S.; Goddard, W. A.; Skiff, W. M. UFF, a Full Periodic Table Force Field for Molecular Mechanics and Molecular Dynamics Simulations. *J. Am. Chem. Soc.* **1992**, *114* (25), 10024−10035.
(52) Fereiro, J. A.; Yu, X.; Pecht, I.; Sheves, M.; Cuevas, J. C.; Cahen, D. Tunneling Explains Efficient Electron Transport via Protein Junctions. *Proc. Natl. Acad. Sci. U. S. A.* **2018**, *115* (20), E4577−E4583.
(53) Shi, W.; Deng, T.; Wong, Z. M.; Wu, G.; Yang, S.-W. A Molecular Roadmap towards Organic Donor-Acceptor Complexes with High-Performance Thermoelectric Response. *Npj Comput. Mater.* **2021**, *7* (1), 1−8.
(54) Warelow, T. P.; Pushie, M. J.; Cotelesage, J. J. H.; Santini, J. M.; George, G. N. The Active Site Structure and Catalytic Mechanism of Arsenite Oxidase. *Sci. Rep.* **2017**, *7* (1), 1757.

https://doi.org/10.1021/acsanm.2c02860
ACS Appl. Nano Mater. 2022, 5, 11876−11888